

*Annual Review of Fluid Mechanics*Submesoscale Dynamics in the
Upper OceanJohn R. Taylor¹ and Andrew F. Thompson²¹Department of Applied Mathematics and Theoretical Physics, University of Cambridge, Cambridge, United Kingdom; email: J.R.Taylor@damtp.cam.ac.uk²Department of Environmental Science and Engineering, California Institute of Technology, Pasadena, California, USA; email: andrewt@caltech.eduANNUAL
REVIEWS **CONNECT**www.annualreviews.org

- Download figures
- Navigate cited references
- Keyword search
- Explore related articles
- Share via email or social media

Annu. Rev. Fluid Mech. 2023. 55:103–27

First published as a Review in Advance on
September 23, 2022The *Annual Review of Fluid Mechanics* is online at
fluid.annualreviews.org<https://doi.org/10.1146/annurev-fluid-031422-095147>

Copyright © 2023 by the author(s). This work is licensed under a Creative Commons Attribution 4.0 International License, which permits unrestricted use, distribution, and reproduction in any medium, provided the original author and source are credited. See credit lines of images or other third-party material in this article for license information.

**Keywords**

ocean, submesoscale, turbulence, eddies, fronts, climate

Abstract

Oceanic motions with spatial scales of 200 m–20 km, called submesoscales, are ubiquitous in the upper ocean and serve as a key intermediary between larger-scale balanced dynamics and unbalanced turbulence. Here, we introduce the fluid dynamics of submesoscales and contrast them with motions at larger and smaller scales. We summarize the various ways in which submesoscales develop due to instabilities that extract potential or kinetic energy from larger-scale balanced currents; some instabilities have counterparts at larger scales, while others are distinct to the submesoscale regime. Submesoscales modify the density stratification in the upper ocean and redistribute energy between scales. These energy transfers are complex, having both up-scale and down-scale components. Submesoscale eddies and fronts also contribute to a spatially heterogeneous distribution of shear and restratification that leave an imprint on upper ocean turbulence. The impact of submesoscales on the Earth's climate remains an exciting research frontier.

1. INTRODUCTION

Photographs taken during early unmanned Apollo missions revealed the presence of spiral-like patterns on the ocean surface in regions of sunglint. These features were later described and cataloged by Paul Scully-Power based on observations made from a flight of the Space Shuttle Challenger in 1984. His insightful mission report reads (Scully-Power 1986, p. 57),

Far and away the most impressive discovery resulting from this flight is the realization that the submesoscale ocean (length scales less than 100 km) is far more complex dynamically than ever imagined in even the least conservative estimates. Moreover, this complexity was seen to extend all the way down (in range) to length scales of 100 meters, yet, on the other hand, patterns of this complexity could be seen to be interconnected for hundreds and hundreds of kilometers.

Several interconnected spirals can be seen in the photograph of sunglint on the Sea of Japan shown in **Figure 1**. The interconnected nature of the features seen across scales from several hundred meters to several hundred kilometers reflects the inherently multiscale nature of the fluid dynamics in the ocean. This review focuses on submesoscale (200 m–20 km) dynamics in the upper ocean with a particular focus on multiscale interactions involving the submesoscale.

Another view of the upper ocean can be seen in the satellite-derived sea surface temperature (SST) from a region of upwelling off the coast of southern California and northern Mexico, shown in **Figure 2**. The patterns in SST suggest coherent eddying motion at two distinct scales. Several large whorls are visible with diameters on the order of 100 km. These are likely signatures of mesoscale eddies, ubiquitous features in the world’s oceans with characteristic sizes between 20 and 200 km. (The term “mesoscale” was inherited from the atmospheric science literature, where this scale range is intermediate between synoptic weather systems and the so-called microscale.)

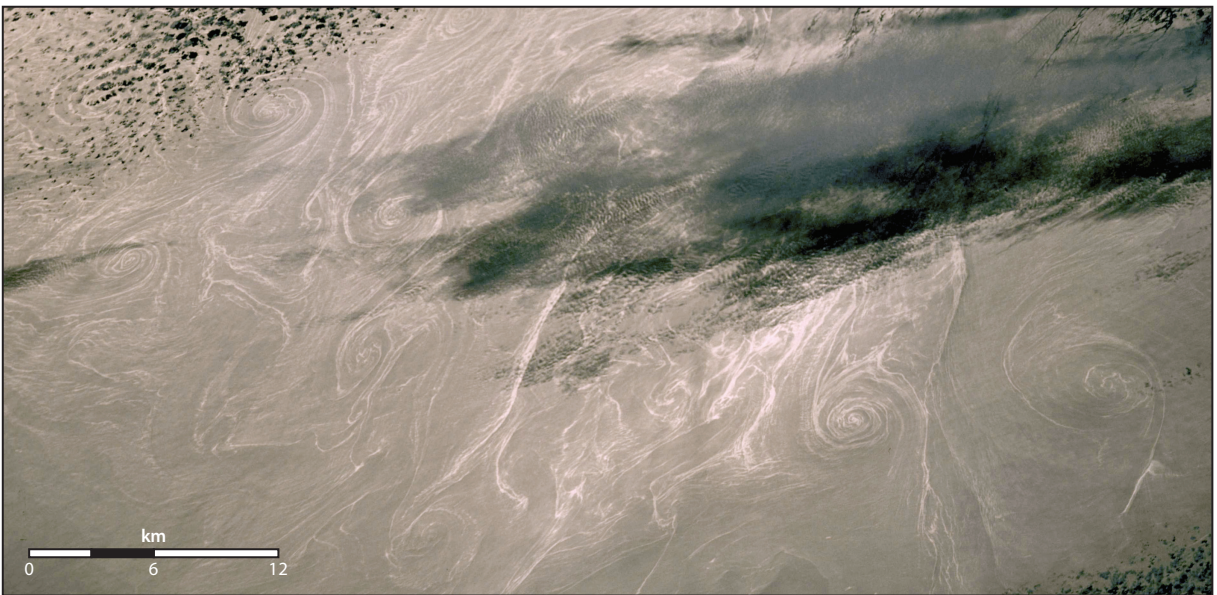


Figure 1

Interconnected spirals visible in a photograph of sunglint on the Sea of Japan taken by astronauts on the Space Shuttle on September 16, 1992. Dark regions are clouds and their shadows. Image courtesy of the Earth Science and Remote Sensing Unit, NASA Johnson Space Center (<https://eol.jsc.nasa.gov>). Scale bar estimated from figure 8 of Munk et al. (2000).

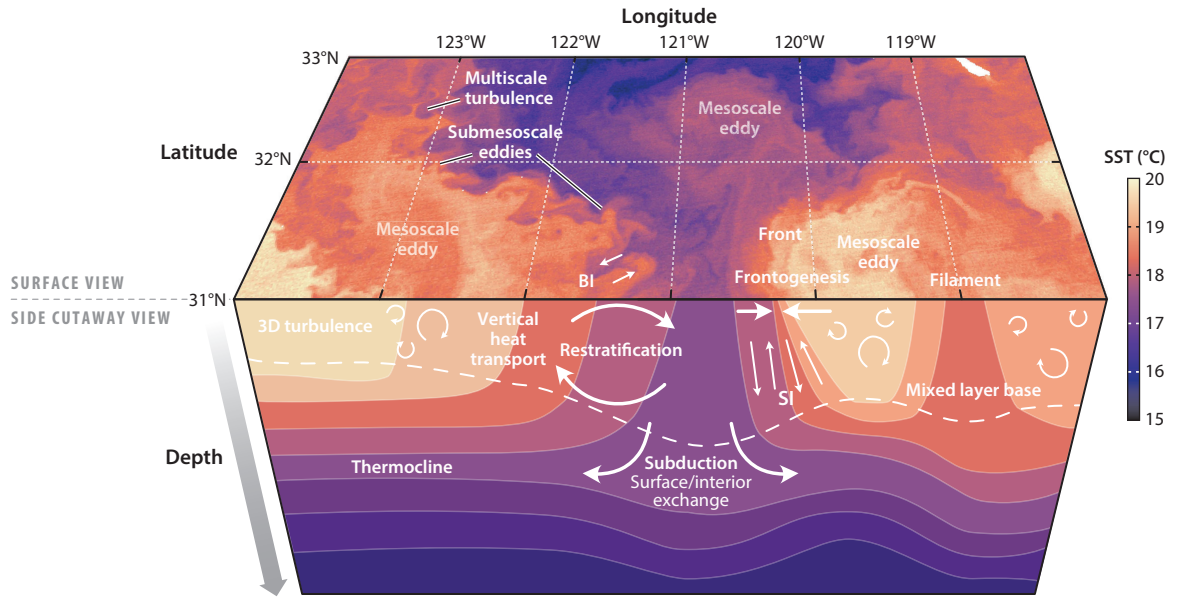


Figure 2

(*Top*, surface view) Sea surface temperature (SST) from NASA MODIS (Moderate-Resolution Imaging Spectroradiometer) Aqua satellite on November 15, 2020. Data from <http://oceancolor.gsfc.nasa.gov>. (*Bottom*, cutaway view) Hypothetical temperature contours illustrating various processes, including submesoscale baroclinic instability (BI) and symmetric instability (SI).

Smaller submesoscale eddies are visible on scales of several kilometers, particularly along temperature fronts and filaments and at the periphery of mesoscale eddies. Other processes discussed in this review are also illustrated in **Figure 2**.

Mesoscale and submesoscale motions can be distinguished by the relative importance of the Earth's rotation. The ratio of the convective and Coriolis accelerations scales with the Rossby number, Ro ,

$$\frac{|\mathbf{u} \cdot \nabla \mathbf{u}|}{|2\boldsymbol{\Omega} \times \mathbf{u}|} \sim \frac{U}{fL} \equiv Ro, \quad 1.$$

where U and L are respectively characteristic horizontal velocity and length scales, $\boldsymbol{\Omega}$ is the Earth's rotation vector, and $f = 2|\boldsymbol{\Omega}| \sin \theta$ is the Coriolis parameter at a latitude θ . Mesoscale eddies are characterized by $Ro \ll 1$, and the dominant terms in the momentum equations are the horizontal pressure gradient and the Coriolis acceleration, such that the flow is close to geostrophic balance. Submesoscales are characterized by $Ro \sim 1$ and, hence, the Coriolis acceleration is important, but it does not constrain the motion to the same extent as the mesoscale. The removal of this constraint allows stronger vertical velocities to develop at submesoscales.

Here, we define submesoscales as dynamical features with horizontal scales between approximately 200 m and 20 km and characterized by $Ro \sim 1$. Submesoscales have received considerable attention in the oceanographic community for the past 15–20 years, and their presence and importance have been highlighted by the advent of high-resolution remote sensing, field measurements, and computational models. Here, we focus on the upper ocean, where submesoscales play a particularly important role in establishing the vertical density stratification, aiding the exchange between surface and interior waters and modulating small-scale turbulence.

Like many problems in fluid dynamics, the vast range of scales associated with oceanic flows make a comprehensive description of ocean dynamics extraordinarily challenging. The large gyres

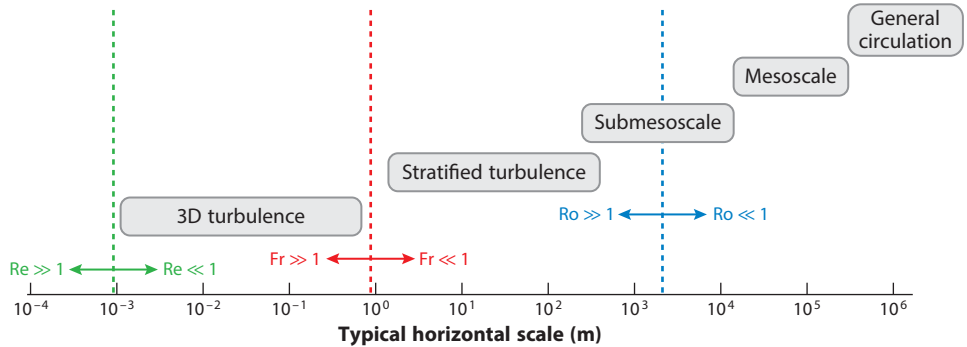


Figure 3

Dynamical regimes and nondimensional parameters [Rossby number Ro , Froude number Fr , and Reynolds number Re (defined in Equation 4)] set against typical horizontal scales. The vertical dashed lines roughly delineate regions where the nondimensional parameters are large or small, although the location of these dividing lines depends on the local conditions. Nominal values of the characteristic buoyancy frequency $N = 10^{-2} \text{ s}^{-1}$ and the Coriolis parameter $f = 10^{-4} \text{ s}^{-1}$ are used to estimate Fr and Ro .

that span ocean basins and the smallest 3D turbulent motions are separated in scale by roughly nine orders of magnitude (**Figure 3**). Even in the most optimistic scenarios, computers will be unable to directly simulate this range of scales in the foreseeable future. It is therefore important to understand the connections between large- and small-scale motions. Submesoscales play a critical role in this dynamical coupling by bridging the gap between rotating and nonrotating flows (that is, those motions that, respectively, are strongly influenced and unaffected by the Earth’s rotation) (McWilliams 2016).

Surface currents in the ocean are primarily driven by wind patterns with scales of $\sim 1,000 \text{ km}$ (i.e., the atmospheric synoptic scale) and larger. Geostrophic turbulence—nonlinear motions with $Ro \ll 1$ (including mesoscale eddies)—on average transfer energy up scale. This raises the question of how the energy input into the ocean is ultimately dissipated. Vigorous turbulence in boundary layers at the top and bottom of the ocean and internal wave generation undoubtedly play a significant role, but submesoscales have also been shown to transfer energy from the mesoscale to small-scale turbulence (Capet et al. 2008c, Naveira Garabato et al. 2022), thereby providing a route for energy to be dissipated.

As they develop, many submesoscale processes increase the vertical density stratification in, or re-stratify, the upper ocean (e.g., Haine & Marshall 1998, Boccaletti et al. 2007). Near the ocean surface, boundary layer turbulence generated by the combined effects of convection, wind stress, and waves maintains the surface mixed layer (ML), a region with nearly uniform properties in the vertical direction. Submesoscale restratification limits the depth to which boundary layer turbulence can penetrate, and in turn reduces the depth of the ML. Shallower and weaker vertical mixing can trigger phytoplankton blooms in light-limited conditions (e.g., Taylor & Ferrari 2011, Mahadevan et al. 2012). The mixed layer depth (MLD) is also an important factor in setting upper ocean dissolved gas concentrations, the rate of air/sea gas exchange, and thus the ocean’s uptake of anthropogenic carbon dioxide (Follows et al. 1996).

Partly due to their nongeostrophic nature, submesoscales are associated with horizontally divergent surface currents and strong vertical velocities (Mahadevan & Tandon 2006). This aids the exchange of water between the ML and the ocean interior. For instance, submesoscale currents can transport deep, nutrient-rich waters toward the surface where light is abundant, enhancing phytoplankton growth (e.g., Lévy et al. 2012, Mahadevan 2016). The vertical motion

ML: (surface) mixed layer

MLD: mixed layer depth

associated with submesoscales also contributes significantly to the heat budget of the upper ocean (Su et al. 2018). Submesoscale downwelling plumes can transport particulates (e.g., microplastics and organic material) into the ocean interior (Omand et al. 2015, Taylor 2018, Taylor et al. 2020).

Many early studies considered submesoscale processes in isolation, either by design (e.g., using idealized numerical experiments) or due to computational or observational constraints. Much of this work has been summarized in several excellent reviews of submesoscale motions and their impact (Thomas et al. 2008; Lévy et al. 2012; Mahadevan 2016; McWilliams 2016, 2019). However, submesoscales also interact with motions on much smaller and larger scales; these multiscale interactions are a main focus of this review. To complement the earlier review articles, we attempt (a) to provide a pedagogical introduction to submesoscale dynamics, aimed at those who have a background in fluid dynamics but are new to the oceanographic community, and (b) to provide a literature survey describing certain multiscale interactions involving submesoscales.

In Section 2 we introduce submesoscales in the context of fluid dynamical processes across a wide range of scales in the ocean. In Section 3 we discuss several fluid dynamical instabilities that give rise to submesoscale features. Finally, we discuss the interaction between submesoscales and small-scale turbulence in the ocean surface boundary layer (Section 4.1) and the influence of submesoscales on larger motions and climate (Section 4.2).

2. MULTISCALE OCEAN FLUID DYNAMICS

The ocean is a rotating, stratified, viscous fluid, but the importance of these effects depends on the scale of motion. To see this, consider the equations of motion in a reference frame rotating with angular velocity $\mathbf{\Omega}$. Using a characteristic velocity scale, U , and length scale, L , the nondimensional incompressible momentum and buoyancy conservation equations can be written as

$$\frac{\partial \mathbf{u}}{\partial t} + \mathbf{u} \cdot \nabla \mathbf{u} = -\frac{P}{\rho_0 U^2} \nabla p + \frac{1}{\text{Fr}^2} b \hat{\mathbf{z}} - \frac{1}{\text{Ro}} \hat{\mathbf{z}} \times \mathbf{u} + \frac{1}{\text{Re}} \nabla^2 \mathbf{u}, \quad 2.$$

$$\frac{\partial b}{\partial t} + \mathbf{u} \cdot \nabla b = \frac{1}{\text{Pr Re}} \nabla^2 b, \quad 3.$$

where time has been normalized with a characteristic advection timescale, L/U . The buoyancy, $b = -g\rho/\rho_0$, has been normalized by $N^2 L$, where $N = \sqrt{\partial b/\partial z}$ is a characteristic buoyancy frequency; ρ is the fluid density, g is the gravitational acceleration, and ρ_0 is a constant reference density under the Boussinesq approximation. The density of seawater depends on temperature and salinity, which diffuse at different rates and have different Prandtl numbers, $\text{Pr} = \nu/\kappa$, where ν is the kinematic viscosity and κ is the molecular diffusivity. However, here we do not consider double diffusion or nonlinearities in the equation of state. Here, $\hat{\mathbf{z}}$ is the local vertical direction (pointing in the direction opposite to gravity). The traditional approximation has also been made by retaining only the vertical component of the angular velocity vector. We also invoke the f -plane approximation by assuming that the Coriolis parameter is constant, which is a good approximation at the submesoscale. The scaling for the characteristic pressure scale, P , will depend on the context of the flow environment.

The nondimensional parameters in the momentum equation are the Froude number, Fr , the Rossby number, Ro , and the Reynolds number, Re , defined as

$$\text{Fr} \equiv \frac{U}{NL}, \quad \text{Ro} \equiv \frac{U}{fL}, \quad \text{Re} \equiv \frac{UL}{\nu}, \quad 4.$$

which quantify the relative importance of buoyancy, rotation, and viscous effects compared to the fluid inertia at a given scale. The effects of density stratification, the Earth's rotation, and viscosity are not directly felt in the momentum equation for $\text{Fr} \gg 1$, $\text{Ro} \gg 1$, and $\text{Re} \gg 1$, respectively.

Dynamical processes in the ocean cover a vast range of length scales and can be categorized into various regimes based on the size of the nondimensional parameters in Equation 4. **Figure 3** illustrates the typical horizontal scales associated with various classes of motion with a rough indication for the corresponding size of Fr , Ro , and Re . All of the processes that we describe here have $Re \gg 1$, and hence, viscous effects do not play a direct role.

At relatively small scales, Fr and Ro are expected to be large and stratification and rotational effects to be weak, and we might expect this scale range to be occupied by 3D turbulence. In stratified parts of the ocean, buoyancy effects are strong ($Fr \ll 1$) for horizontal scales larger than ~ 1 m. In weakly stratified boundary layers, the scale at which stratification effects become important could be larger, and stratification effects will be important for motions whose scale is comparable to the thickness of the boundary layer. For scales smaller than a few hundred meters, rotational effects are weak ($Ro \gg 1$). The scale range of $Re \gg 1$, $Fr \ll 1$, and $Ro \gg 1$ is occupied by stratified turbulence, as reviewed by Riley & Lelong (2000), Riley & Lindborg (2008), and Caulfield (2021). For scales larger than about 10 km, the Rossby number is also small ($Ro \ll 1$) and, hence, both stratification and rotation constrain the motion. This includes ~ 100 -km mesoscale eddies and the major global current systems [e.g., western boundary currents, ocean gyres, and the Antarctic Circumpolar Current (ACC)] that make up the general circulation. The dynamics on these scales have traditionally been described by asymptotic theories that use the Rossby number as a small parameter.

Submesoscales occupy a scale range where $Ro \sim 1$ and, hence, where the Earth's rotation is important but does not constrain the motion as strongly as it does at larger scales. Buoyancy effects also play an important role at these scales, and as will be discussed below, submesoscales in the upper ocean are strongly influenced by the thickness of the ML. The scales with $Fr \ll 1$, including submesoscales, are highly anisotropic, where the characteristic vertical scale is small compared to the horizontal scale. Stratified turbulence and submesoscales typically develop in such a way that the vertical Froude number is $Fr_v \equiv U/NH \sim 1$, where H is a characteristic vertical length scale (Lindborg 2006, Boccaletti et al. 2007).

In quasi-balanced theories that are valid for $Ro \ll 1$, the horizontal motion is nearly nondivergent, and thus vertical velocities are small. A consequence of the loosening of the rotational constraint at submesoscales is that strong vertical motion can develop at these scales. **Figure 4** illustrates the typical aspect ratio and Rossby number associated with mesoscale eddies, submesoscales, and 3D turbulence, along with scalings for the horizontal (U) and vertical (W) velocities. For isotropic turbulence the aspect ratio is ~ 1 (by definition) and we have $W \sim U$. Mesoscale eddies have a small aspect ratio, and the vertical velocity is further limited by the small Rossby number (Mahadevan et al. 1996). Although submesoscales are characterized by a relatively small aspect ratio, $H/L \sim 10^{-2}$, the vertical velocity is not subject to the additional Rossby number constraint; hence, we have $W/U \sim 10^{-2}$, which is 10–100 times larger than that of the mesoscale (Mahadevan & Tandon 2006).

A remarkable feature of ocean dynamics is that the characteristic horizontal velocity scale associated with the processes illustrated in **Figure 3** is roughly 0.1–1 m/s, despite the fact that the characteristic horizontal length scales span about eight orders of magnitude. We can estimate the vertical velocity associated with each process using a characteristic horizontal velocity of $U = 0.1$ m/s (**Figure 4**). While mesoscale eddies are typically associated with vertical velocities of 1–10 m/day, the vertical velocity associated with submesoscale motions can exceed 100 m/day. This is significant at least in part because the time for submesoscale motions to transport material across the ML (~ 1 day) is comparable to the response time for marine microorganisms, and as a result, submesoscale vertical motions have a strong impact on ocean biology (Lévy et al. 2012).

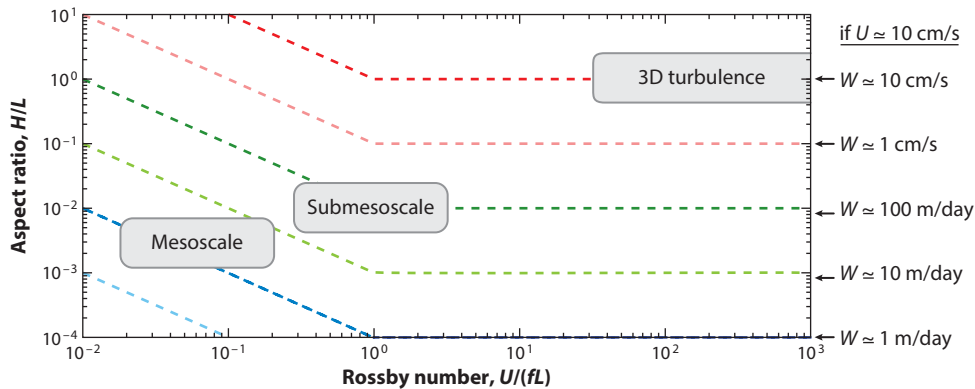


Figure 4

Typical aspect ratio H/L (for a characteristic vertical scale, H , and horizontal scale, L) and Rossby numbers $Ro = U/(fL)$ associated with mesoscale eddies, submesoscales, and 3D turbulence. Scalings for the ratio of characteristic vertical (W) and horizontal (U) velocities are shown in dashed lines: $W/U \sim Ro(H/L)$ for $Ro < 1$ (from Mahadevan et al. 1996) and $W/U \sim H/L$ for $Ro > 1$. Typical dimensional vertical velocities are also indicated along the right edge of the figure for a horizontal velocity scale of 10 cm/s.

3. SUBMESOSCALE INSTABILITIES

3.1. Introduction

Ocean fronts—elongated regions with large horizontal buoyancy gradients—occur on a variety of horizontal scales. On large scales, persistent fronts are associated with the large-scale currents that make up the general circulation (e.g., the Gulf Stream). Fronts also evolve as ephemeral features and form via the intensification of preexisting buoyancy gradients in a process called frontogenesis (**Figure 2**). Fronts provide a key source of energy for submesoscale currents through a zoo of dynamical instabilities (Thomas et al. 2008). These include horizontal shear instabilities (Munk et al. 2000), baroclinic instability (BI) (Eldevik & Dysthe 2002, Boccaletti et al. 2007), symmetric instability (SI) (Taylor & Ferrari 2010), inertial instability (II) (or centrifugal instability) (Gula et al. 2016), and ageostrophic anticyclonic instability (AAI) (McWilliams et al. 2004). In this section we discuss submesoscale instabilities for idealized flows and emphasize the connections between various instability mechanisms.

On sufficiently large scales such that $Ro \ll 1$, $Fr \ll 1$, and $H/L \ll 1$, the ocean is maintained in a state that is close to hydrostatic and geostrophic balance. The combination of hydrostatic and geostrophic balance implies that a vertically sheared horizontal current known as the thermal wind balances horizontal buoyancy gradients:

$$\underbrace{\frac{1}{\rho_0} \frac{\partial p}{\partial z} = b}_{\text{hydrostatic balance}}, \quad \underbrace{f \hat{\mathbf{z}} \times \mathbf{u} = -\frac{1}{\rho_0} \nabla_h p}_{\text{geostrophic balance}} \quad \rightarrow \quad \underbrace{-f \hat{\mathbf{z}} \times \frac{\partial \mathbf{u}}{\partial z} = \nabla_h b}_{\text{thermal wind balance}} \quad 5.$$

where $\nabla_h = (\partial_x, \partial_y, 0)$ is the horizontal gradient operator. Observations have confirmed that large-scale ocean fronts are close to a state of thermal wind balance (Rudnick & Luyten 1996), and this balance is a good approximation for motions at the mesoscale or larger, where $Ro \ll 1$. At the submesoscale, the dynamical equilibrium in Equation 5 is often unstable. Thermal wind balance can also be modified by other factors. For curved submesoscale fronts with $Ro \sim 1$, the centrifugal acceleration can also be important in what is called cyclogeostrophic balance (Shakespeare 2016).

BI: baroclinic instability

SI: symmetric instability

II: inertial instability

AAI: ageostrophic anticyclonic instability

As discussed in Section 4.1, turbulent mixing can disrupt thermal wind balance by reducing the vertical shear.

In an inviscid, adiabatic fluid in a rotating reference frame, the potential vorticity (PV) is conserved by the fluid motion, where PV is

$$\text{PV} \equiv (f\hat{\mathbf{z}} + \boldsymbol{\omega}) \cdot \nabla b, \quad 6.$$

and $\boldsymbol{\omega} = \nabla \times \mathbf{u}$ is the relative vorticity. The PV is a valuable tool to diagnose and understand submesoscale instabilities and their influence on upper ocean dynamics.

Submesoscale instabilities draw their energy from potential energy and kinetic energy (KE) reservoirs. The minimum potential energy that can be reached via adiabatic rearrangement of fluid parcels corresponds to flat density surfaces (isopycnals). Other states, including those with tilted isopycnals, have additional, available potential energy (APE) (Lorenz 1955, Winters et al. 1995) that can fuel submesoscale motions. Furthermore, submesoscales can grow by drawing from KE associated with the thermal wind. The vertical and horizontal shear associated with balanced fronts can generate submesoscale currents through vertical and horizontal shear production, respectively. In both cases, KE associated with the thermal wind is reduced, which disrupts thermal wind balance and causes the now unbalanced pressure gradient to flatten isopycnals.

Regardless of the energy pathway, submesoscale instabilities developing from a state of thermal wind balance tend to decrease the total energy (KE plus APE) in the frontal system, which is associated with mesoscale or larger motions. Thus, submesoscale instabilities represent a down-scale transfer of energy (Capet et al. 2008c). Some of this energy will be transferred to still smaller scales through secondary instabilities, submesoscale frontogenesis, and 3D turbulence (see Section 4.1).

Below, we discuss two groups of submesoscale instabilities that develop from idealized basic states: submesoscale analogs of balanced instabilities, and inherently ageostrophic instabilities that do not occur for $\text{Ro} \ll 1$.

3.2. Balanced Instabilities in Idealized Models

Here, we consider submesoscale instabilities using a series of idealized models with a basic state characterized by uniform horizontal and vertical buoyancy gradients in thermal wind balance and bounded by horizontal surfaces. Specifically, the basic state buoyancy and velocity are $b = M^2 x + N^2 z$ and $v = M^2 z/f$, where f is the Coriolis parameter, M^2 is defined as $\partial b/\partial x$, and f, M, N , and $\text{PV} \equiv fN^2 - M^4/f$ are constant.

Perhaps the simplest model of upper ocean dynamics consists of a uniform PV fluid bounded from above by a horizontal plane at $z = 0$, representing the ocean surface. In the limit of $\text{Ro} \ll 1$, this is the surface quasi-geostrophic (SQG) model introduced by Held et al. (1995). Since PV is conserved in an inviscid, adiabatic fluid, the interior PV remains constant in the SQG model, and the evolution of the system is dictated by the surface buoyancy (at $z = 0$). For the basic state given above, the SQG model supports stable, linear Eady edge waves that decay exponentially with depth (**Figure 5**).

Despite its simplicity, nonlinear flows in the SQG model reproduce some aspects of upper ocean dynamics. In an analog to the nonlinear behavior of vorticity in 2D turbulence, large buoyancy gradients develop at the surface due to stirring by large-scale motions (Lapeyre & Klein 2006, Lapeyre et al. 2006), and these fronts and filaments can become unstable and roll up into eddies (Held et al. 1995). A similar process was invoked by Munk et al. (2000), who hypothesized that horizontal shear instabilities, acting preferentially on cyclonic vorticity filaments, lead to the submesoscale spiral eddies seen from space (**Figure 1**). However, using linear theory and observations from the North Atlantic, Buckingham et al. (2017) concluded that the observed submesoscale

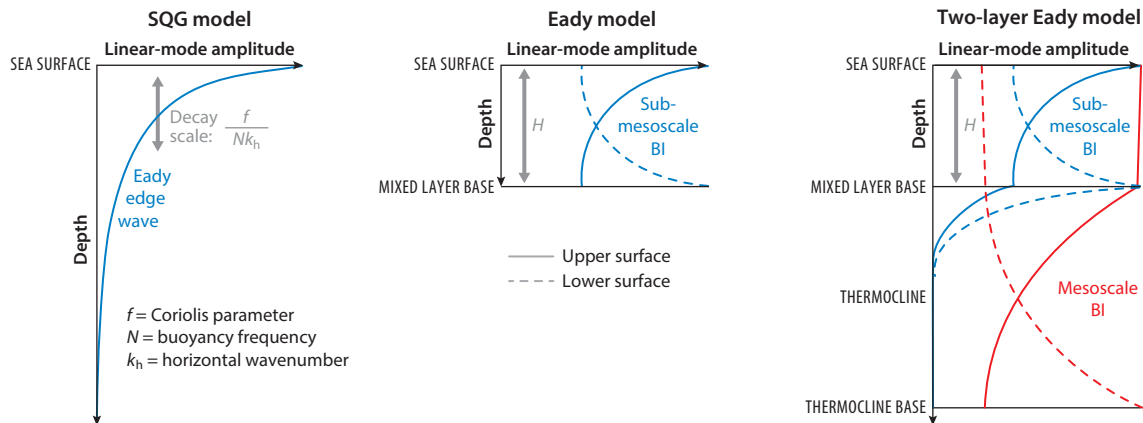


Figure 5

Three models for studying submesoscale instabilities in the upper ocean: surface quasi-geostrophic (SQG), Eady, and two-layer Eady (see discussion in Section 3.2). Curves indicate the vertical structure of linear perturbations to a frontal zone basic state with uniform horizontal and vertical buoyancy gradients in thermal wind balance. Baroclinic instability (BI) develops in the Eady model and the two-layer Eady model via the interaction of Eady edge waves associated with buoyancy anomalies on the upper and lower surfaces. Two-layer Eady model profiles based on Callies et al. (2016), figure 3.

eddies were more likely generated by a different mechanism, BI, as first suggested by Eldevik & Dysthe (2002).

BI was discovered by Charney (1947) and Eady (1949) as an explanation for the development of mid-latitude weather systems. To represent BI in the upper ocean, we need to include the base of the ML, or allow the PV of the fluid to vary. The Eady model consists of a constant PV fluid bounded by two rigid horizontal surfaces (Figure 5). BI develops by converting APE from the basic state into perturbation KE. After disturbances grow and become nonlinear, they roll up into eddies whose horizontal size is inherited from the wavelength of the unstable modes (Tulloch et al. 2011). BI develops in the Eady model when Eady edge waves at the top and bottom surfaces phase lock and grow. For $Ro \ll 1$, the horizontal size of the fastest-growing perturbations is proportional to the deformation scale, NH/f , where H is the vertical extent of the fluid layer (Eady 1949).

Submesoscale BI in the ML, sometimes termed mixed layer instability (MLI), can be represented by the Eady model, where the top and bottom surfaces correspond to the ocean surface and the base of the ML, respectively. However, since submesoscales are characterized by $Ro \sim 1$, growing perturbations might depart from the state of geostrophic balance that was assumed by Eady (1949). In a series of papers, Stone (1966, 1970, 1972) analyzed nongeostrophic perturbations in the Eady model. For small Ro , disturbances grow slowly compared to the timescale associated with rotation, as in Eady's (1949) analysis. However, for $Ro \sim 1$, the growth rate becomes comparable to f ; hence, submesoscale eddies can develop within a few days. Stone's analysis of the nongeostrophic Eady problem also includes SI, which is discussed in Section 3.3.

The Eady model is also useful for examining nonlinear submesoscale dynamics. Molemaker et al. (2010) compared simulations of the Eady model using the nongeostrophic Boussinesq equations and the quasi-geostrophic (QG) equations (which assume $Ro \ll 1$). In both cases, eddies develop through BI on a scale close to the ML deformation scale, NH/f . In the QG system, most of the energy remains at large scales, and energy dissipation is weak. However, in the nongeostrophic simulations, small 3D turbulence develops along buoyancy fronts and KE is removed through viscosity and mixing at small scales. This was one of the first demonstrations that submesoscales can generate 3D turbulence, providing a route for the dissipation of energy in balanced flows.

While the Eady model can capture BI, SQG-like dynamics, and frontogenesis, it cannot simultaneously capture submesoscale and mesoscale BI. A simple model that includes both flavors of BI consists of two vertically stacked fluid layers with uniform PV, separated by a deformable interface—the two-layer Eady model (Blumen 1979, Callies et al. 2016). In the context of the upper ocean, the top and bottom layers in the two-layer Eady model correspond to the weakly stratified ML and the thermocline, respectively (**Figure 5**). In the two-layer model, Eady edge waves are supported at each of the three bounding surfaces. For parameters typical of the upper ocean, the most unstable mode corresponds to submesoscale BI, which involves coupled Eady edge waves at the ocean surface and the base of the ML (Callies et al. 2016). Submesoscale modes in the ML are effectively decoupled from the base of the thermocline, which helps explain why key aspects of submesoscale BI can be captured by the single-layer Eady model. However, submesoscale perturbations can extend into the thermocline and stir tracers there (Badin et al. 2011). Interestingly, the decay of submesoscale modes in the thermocline is qualitatively similar to the decay of synoptic modes in the stratosphere (see figure 2 in Eady 1949). This suggests that the vertical structure of submesoscale eddies in the ocean is analogous to synoptic weather systems in the atmosphere, although it is worth emphasizing that the Rossby number associated with submesoscale eddies is $Ro \sim 1$, while synoptic scales in the atmosphere have $Ro \ll 1$.

3.3. Nongeostrophic Submesoscale Instabilities

The second class of submesoscale instabilities only appear for finite Rossby number and hence do not have a geostrophic analog. Some of these inherently nongeostrophic instabilities can be viewed as the unstable counterpart to internal waves in a rotating, stratified fluid, including II and SI, which generate motions in the submesoscale range.

Following Hoskins (1974), these instabilities and the relationship between them can be illustrated by considering periodic disturbances to a basic state with constant buoyancy and velocity gradients: $b_z = N^2$, $b_x = M^2$, $v_z = M^2/f$, and $v_x = \zeta$, where subscripts denote partial differentiation. Small-amplitude perturbations of the form

$$w = \widehat{w} e^{i(kx + mz - \omega t)} \quad 7.$$

that are independent of the along-front (y) direction satisfy the dispersion relation:

$$\omega^2 = \frac{m^2 f (f + \zeta)}{k^2 + m^2} + \frac{k^2 N^2}{k^2 + m^2} - \frac{2kmM^2}{k^2 + m^2}. \quad 8.$$

For $\omega^2 > 0$, Equation 8 is the dispersion relation for linear plane waves in a baroclinic ($M^2 \neq 0$), rotating, stratified fluid, and exponentially growing perturbations develop for $\omega^2 < 0$. For $N^2 = M^2 = 0$, II develops for $f(f + \zeta) < 0$ or, equivalently, when ζ takes the opposite sign from f (it is anticyclonic) and $|\zeta| > |f|$. Note that the term “centrifugal instability” is sometimes used in this context (e.g., McWilliams 2016). We avoid this term since the basic state consists of a balance between the Coriolis acceleration and the pressure gradient and does not generally involve the centrifugal acceleration, and since II can be viewed as the unstable counterpart to inertial waves.

Unstable modes in this system with $f(f + \zeta) > 0$ and $N^2 > 0$ are often termed SI. The horizontal buoyancy gradient (M^2) increases the likelihood of instability. The most unstable modes have $km > 0$ for $M^2 > 0$ or $km < 0$ for $M^2 < 0$, such that the phase lines of the unstable perturbations are tilted in the direction of the isopycnals. In the hydrostatic limit (with $k^2 \ll m^2$), the most unstable mode of SI in this unbounded system is aligned with isopycnals. As such, the buoyancy perturbations and buoyancy flux associated with SI are typically small and SI derives its energy from the thermal wind shear (Stone 1972).

As first shown by Hoskins (1974), SI and II can develop when the PV takes the opposite sign to f (such that $fPV < 0$). Comparison of the conditions for II [$f(f + \zeta) < 0$] and SI [$f(\mathbf{k} + \boldsymbol{\omega}) \cdot \nabla b < 0$] shows that SI can be viewed as II in a coordinate system aligned with the sloping isopycnals. Hence, an alternative name for SI could be “slantwise inertial instability.” The fact that the condition for SI depends on a materially conserved quantity (PV) presents a paradox: No reconfiguration of the fluid parcels within an unstable region will stabilize the flow. Several possible resolutions to this paradox were discussed by Thorpe & Rotunno (1989). Taylor & Ferrari (2009) found that secondary Kelvin–Helmholtz instabilities that develop from the primary SI bands cure the instability by either entraining nearby fluid with $fPV > 0$ or inducing stabilizing viscous/diffusive fluxes of PV at the sea surface. As discussed in Section 4.1, the secondary instabilities energize small-scale turbulence and provide a route for energy to be dissipated.

Another nongeostrophic submesoscale instability, termed AAI (McWilliams et al. 2004, Molemaker et al. 2005), can develop for $f(f + \zeta - S) < 0$, where $S = \sqrt{(u_x - v_y)^2 - (u_y + v_x)^2}$ is the horizontal strain rate (McWilliams 2016). A form of AAI is present in the Eady model (Molemaker et al. 2005), although it is subdominant since its growth rate is always smaller than either BI or SI. Although there is not a critical Rossby number required for AAI, its growth rate is exponentially small for small Ro, and hence, it is only likely to appear for moderate Ro associated with submesoscales (Molemaker et al. 2005). AAI has analogs in stratified Taylor–Couette flow (Molemaker et al. 2001, Yavneh et al. 2001) and in the shallow-water equations (Satomura 1981, Griffiths et al. 1982).

3.4. Restratification by Submesoscale Instabilities

Submesoscales develop by extracting potential or kinetic energy associated with balanced horizontal buoyancy gradients and horizontally sheared currents. This ultimately increases the vertical buoyancy gradient of, or restratifies, the upper ocean. Parameterizations for submesoscale BI (Fox-Kemper et al. 2008, Canuto & Dubovikov 2010, Brüggemann & Eden 2014), SI (Bachman et al. 2017b) and horizontal shear instabilities (Bachman et al. 2017a) have been developed, but to our knowledge, parameterizations do not yet exist for II or AAI. Restratification induced by submesoscales competes with the tendency for boundary layer turbulence to keep the upper ocean well mixed.

The processes that influence upper ocean stratification can be illustrated using the depth-integrated, Reynolds-averaged buoyancy equation:

$$\frac{\partial}{\partial t} \left[\int_z^0 \bar{b} dz \right] = -M^2 \int_z^0 \bar{u} dz + \overline{w'b'} + B_0, \quad 9.$$

where $(\bar{\cdot})$ denotes a horizontal average; departures from this average, denoted with primes, are assumed to be horizontally homogeneous; and $M^2 = \partial \bar{b} / \partial x$ is a large-scale mean buoyancy gradient. The mean buoyancy in the upper ocean can change owing to a mean cross-front flow \bar{u} , the vertical buoyancy flux $\overline{w'b'}$, and the surface buoyancy flux B_0 .

When a persistent wind blows over a front, it will induce an advective Ekman buoyancy flux (EBF). A steady surface wind stress induces a depth-integrated Ekman transport to the right of the wind in the Northern Hemisphere (e.g., Kundu et al. 2015). When the integral in Equation 9 encompasses the full Ekman layer depth and the Reynolds-averaged flow is steady, the first term on the right-hand side is the EBF, written more generally as

$$EBF = \left(\frac{\boldsymbol{\tau} \times \hat{\mathbf{z}}}{\rho_0 f} \right) \cdot \nabla_h b, \quad 10.$$

where τ is the wind stress. Thomas (2005) showed that a frictional surface PV flux arises when the wind stress has a component that is down front (i.e., in the direction of the thermal wind), which reduces fPV .

Submesoscale BI restratifies the upper ocean through the vertical buoyancy flux, $\overline{w'b'}$ in Equation 9 (Stone 1972). BI generates motion that carries light water ($b' > 0$) up and dense water ($b' < 0$) down such that $\overline{w'b'} > 0$. Fox-Kemper et al. (2008) parameterized the mean restratification by submesoscale BI using an advective streamfunction with flow in the cross-front/vertical plane:

$$\overline{w'b'}\Big|_{z=-H/2} = M^2 \int_{-H/2}^0 \bar{u} dz = M^2 \psi|_{z=-H/2} = \frac{c_e H^2 M^4}{f}, \quad 11.$$

where c_e is an empirical coefficient and H is the MLD.

The competition between restratification by submesoscale BI and mixing due to convection and down-front winds can be assessed using a ratio of buoyancy fluxes (Mahadevan et al. 2010, 2012; Callies & Ferrari 2018b):

$$R \equiv \frac{f(B_0 + EBF)}{H^2 M^4} = \left(\frac{w_*^3}{\Delta V_G^3} + \frac{v_*^2}{\Delta V_G^2} \right) \left(\frac{M^2}{f^2} \right), \quad 12.$$

where the coefficient c_e has been omitted following Taylor (2016) and Callies & Ferrari (2018b), $w_* \equiv (B_0 H)^{1/3}$ is the convective velocity scale, $v_* \equiv (\tau_y / \rho_0)^{1/2}$ is the friction velocity associated with the along-front wind stress, and $\Delta V_G \equiv M^2 H / f$ is the change in thermal wind over the ML. For $R \gg 1$, turbulent mixing is expected to overcome restratification by submesoscale BI, and for $R \ll 1$, submesoscale BI will tend to restratify the upper ocean.

When the density of water at the surface of the ocean increases due to surface cooling or evaporation or through advection associated with down-front winds, a convective layer develops where the vertical buoyancy flux, $\overline{w'b'}$, is positive. At sufficiently strong fronts, SI can develop and maintain stable stratification below the convective layer of depth b and above the full boundary layer depth H . The ratio of the convective layer depth to the MLD satisfies (Taylor & Ferrari 2010, Thomas et al. 2013, Callies & Ferrari 2018a)

$$\left(\frac{b}{H} \right)^4 - c^3 \left(1 - \frac{b}{H} \right)^3 R^2 \frac{f^4}{M^4} = 0, \quad 13.$$

where $c \simeq 14$ is an empirical scaling coefficient and R is the restratification ratio defined in Equation 12. We can view the competition between restratification by submesoscale SI and BI and turbulent mixing in a single framework as a function of R and the normalized frontal strength, $M^2 / f^2 = |\nabla_h b| / f^2$, as illustrated in **Figure 6**. For $b/H < 0.5$ (above the diagonal line in **Figure 6**), SI maintains stable stratification in the region $-H < z < -b$ (Taylor & Ferrari 2010), and for $R < 1$, BI outcompetes the surface forcing and restratifies the ML. **Figure 6** is largely based on simulations that isolated SI and BI, so the regime boundaries are speculative. However, Verma et al. (2022) showed that BI and SI coexist in the presence of surface cooling for parameters consistent with **Figure 6**. Note that SI is only capable of restratifying the ML to a state of marginal stability with $fPV \simeq 0$ (Taylor & Ferrari 2010), while BI can lead to significantly stronger stratification (Callies & Ferrari 2018b). However, SI restratifies significantly faster than BI, and hence, SI can quickly respond to strong forcing events (Thomas et al. 2016). Further work is needed to understand the connections between SI, BI (and other submesoscale instabilities), and boundary layer turbulence.

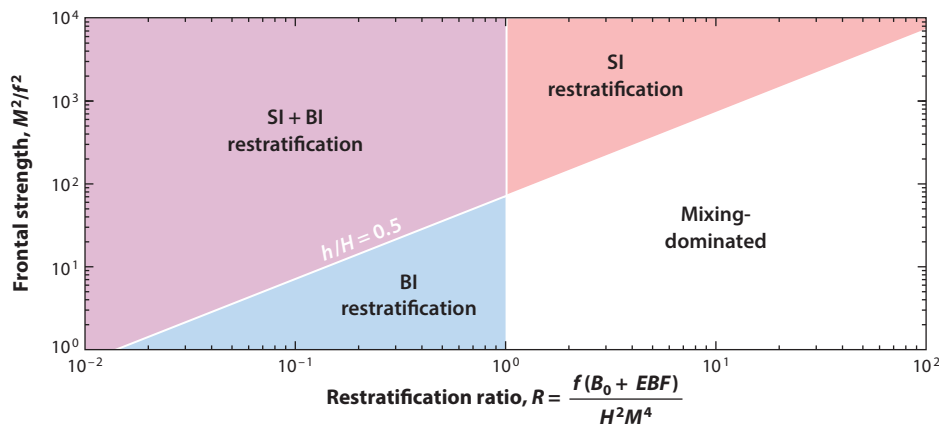


Figure 6

Anticipated result of the competition between submesoscale restratification and turbulent mixing in the upper ocean. The restratification ratio, R , is defined in terms of the Coriolis parameter, f , the surface buoyancy flux, B_0 , the Ekman buoyancy flux, EBF , the mixed layer depth, H , and the horizontal buoyancy gradient, M^2 . The labels indicate where symmetric instability (SI), baroclinic instability (BI), or both (SI + BI) are expected to maintain stable stratification in the upper ocean or where mixing from convection and down-front winds maintains a well-mixed layer. SI is anticipated for $b/H < 0.5$ (above the white labeled line), where b is the convective layer depth.

4. MULTISCALE INTERACTIONS INVOLVING THE SUBMESOSCALE

Recent work has shown that submesoscales link the large-scale circulation with small-scale turbulence through a variety of multiscale interactions, some of which are illustrated in **Figure 7**. Here, we survey this rapidly developing area, first considering the close connections

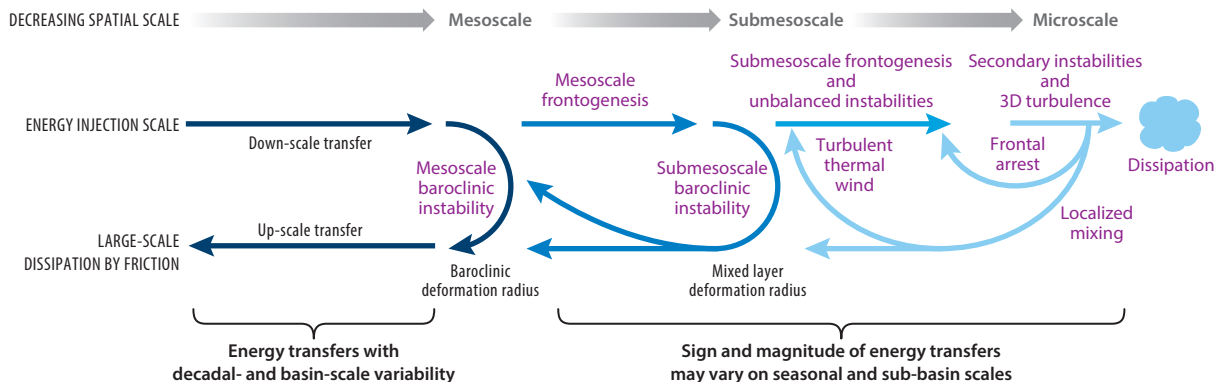


Figure 7

Multiscale interactions and oceanic energy transfer. The transfer of energy to scales smaller than the first baroclinic deformation radius by mesoscale frontogenesis is an important step in down-scale transfer of energy toward dissipative scales (Section 4.1). However, energy residing at submesoscales may be transferred in the net either up scale or down scale due to various dynamical processes (*purple text*). The relative partitioning of energy moving to smaller or larger scales is, at submesoscales, likely to vary both regionally within basins and temporally over seasonal timescales and remains an area of open research (see further discussion in Section 4.2). This figure builds on previous schematics by Salmon (1980) (mesoscale and larger scales) and McWilliams (2016) (down-scale route only), but does not include the contribution from internal waves, which were reviewed recently by Sutherland et al. (2019).

between submesoscales and small-scale turbulence (Section 4.1), followed by a discussion of submesoscale impacts on the large-scale circulation and the climate system (Section 4.2).

4.1. Down-Scale Connections

Observations of coherent submesoscale features (e.g., McWilliams 1985) preceded an increased interest in their global impact in the late 2000s, spurred on by the potential for this class of motions to reconcile the ocean's global energy budget (Capet et al. 2008c, Klein et al. 2008). Energy enters the ocean predominantly at large ($\gtrsim 1,000$ km) scales through surface wind and buoyancy forcing and undergoes a down-scale transfer to ~ 100 -km scales, where mesoscale BI converts the energy to low vertical modes (eigenfunctions of the linearized equations of motion). Energy in these low modes is thought to move preferentially up scale due to an inverse cascade in 2D or geostrophic turbulence (Salmon 1980), which is incompatible with observational evidence that energy removal largely occurs via turbulent dissipation at small scales (Wunsch & Ferrari 2004).

Submesoscale motions were highlighted as potential mechanisms for supplying energy from the ocean mesoscale to small-scale turbulence and ultimately dissipation scales (Ferrari & Wunsch 2009, McWilliams 2016). Early numerical simulations that permitted a rich mesoscale eddy field but also resolved dynamics down to ~ 1 km (e.g., Capet et al. 2008b,c; Klein et al. 2008) indicated that the formation of fronts and submesoscale instabilities provides a path for energy to move to smaller scales. Submesoscale eddies drive further frontogenesis (Barkan et al. 2019), forming submesoscale fronts and filaments where shear instabilities generate intense small-scale turbulence (Molemaker et al. 2010, Skillingstad & Samelson 2012, Stamper & Taylor 2017, Sullivan & McWilliams 2018, Verma et al. 2019), completing the journey from large-scale balanced motion to unbalanced small-scale turbulence. Small-scale turbulence is also intrinsically linked with SI, where the energy extracted from the thermal wind shear is converted to small-scale turbulence through secondary shear instabilities (Taylor & Ferrari 2009, 2010).

These modeling studies inspired the design of field programs that sought evidence for enhanced dissipation due to submesoscales. Early field work focused on regions of intense mesoscale activity (e.g., western boundary currents, upwelling zones, and the ACC), where mesoscale frontogenesis and enhanced vorticity ensured flow conditions with $Ro \sim 1$, as well as strong lateral density gradients. By measuring small (< 10 cm) temperature fluctuations, Johnston et al. (2011) found enhanced turbulent mixing rates on the dense side of a front in the California Current (located slightly north of the region depicted in **Figure 2**). A semi-Lagrangian survey at the Kuroshio front (D'Asaro et al. 2011) revealed that alignment of surface winds with frontal currents produced a negative EBF (Section 3.3) that generated strong vertical motion and elevated dissipation. Based on observations and simulations of the Gulf Stream, Thomas et al. (2016) found that SI, excited by a brief period of down-front winds, extracted and ultimately dissipated energy associated with the large-scale balanced front. In a region of more moderate mesoscale KE in the North Atlantic, a year-long estimate of dissipation rates from ocean gliders exhibited more high-frequency variability than expected from 1D turbulence closure models. The periods of enhanced variability coincided with evidence of active submesoscale instabilities (Evans et al. 2018), which are not captured in the 1D models. An analysis of moored observations from the same location found that the contribution to turbulent dissipation rates in the surface boundary layer from submesoscales was relatively small, but other processes, such as SI, could be a significant sink of energy for the background geostrophic (gyre) circulation (Buckingham et al. 2019).

In the upper ocean, wind, waves, and convection generate boundary layer turbulence to a depth that is often limited by the stable stratification at the base of the ML. Submesoscales have an indirect influence on the depth and intensity of boundary layer turbulence by restratifying the ML. Ocean models often have insufficient resolution to capture boundary layer turbulence and hence

account for its influence with various parameterizations. Perhaps as a result, early work focused on the tendency for submesoscales to reduce the MLD (e.g., Thomas et al. 2008, Fox-Kemper et al. 2008).

Although the net effect of submesoscale eddies has been parameterized using an overturning streamfunction that depends on bulk parameters (Equation 11) (Fox-Kemper et al. 2008), on the scale of an individual eddy, submesoscale restratification is highly nonuniform. For example, in simulations of submesoscale BI with surface cooling by Akitomo (2010), uplifted isopycnals with strong stratification developed within cyclonic submesoscale eddies that were surrounded by sharp submesoscale fronts. More recent high-resolution simulations have shown that submesoscales strongly modulate thermal convection (Taylor 2016, Callies & Ferrari 2018a, Verma et al. 2022). A qualitatively similar picture was seen in large-eddy simulations by Whitt & Taylor (2017), who found that the squared buoyancy frequency (N^2) can vary by about a factor of 10 in the lower portion of the ML following a strong forcing event, and Whitt et al. (2019) found that the resulting patchwork of enhanced and reduced mixing triggered a phytoplankton bloom. Submesoscales also modulate so-called Langmuir turbulence, which is generated through a combination of wind and surface waves (Hamlington et al. 2014, Skillingstad et al. 2017).

The localization of boundary layer turbulence catalyzes submesoscale BI, forming a feedback loop (**Figure 7**). Controlled simulations with and without surface forcing have shown that boundary layer turbulence enhances APE extraction by submesoscale BI (Hamlington et al. 2014, Whitt & Taylor 2017, Verma et al. 2022). Mixing by small-scale turbulence also has an important but indirect impact on submesoscales by influencing the MLD, which then sets the size of the KE and APE reservoirs that are available for submesoscale instabilities. Deeper MLs provide more APE for BI and expose more of the thermal wind shear to possible extraction through SI.

The sensitivity to MLD produces a strong seasonal cycle in submesoscale activity. Capet et al. (2008a) found elevated submesoscale KE in the fall and winter over the Argentinian shelf. They concluded that a combination of deep MLs and large horizontal buoyancy gradients led to larger APE extraction via BI, which is qualitatively consistent with the parameterization of Fox-Kemper et al. (2008). Similarly, Mensa et al. (2013) and Callies et al. (2015) noted much more energetic submesoscales during winter in the vicinity of the Gulf Stream using simulations and observations, respectively. Brannigan et al. (2015), Buckingham et al. (2016), and Thompson et al. (2016) found evidence of enhanced submesoscale SI and BI in a region of the northeastern Atlantic Ocean that did not include permanent frontal systems, suggesting that submesoscales are broadly active in the winter in the open ocean.

The criteria for BI and SI depend on the MLD and the magnitude of the horizontal buoyancy gradient, suggesting that sufficiently strong fronts can support enhanced submesoscale activity throughout the year, irrespective of the MLD. For example, the simulations of Barkan et al. (2017) exhibited enhanced submesoscale activity along the Mississippi–Atchafalaya River plume in the northern Gulf of Mexico in summer. Since the size of submesoscale features scales with the MLD, submesoscales are very difficult to resolve in models in shallow summer MLs (Barkan et al. 2017, Dong et al. 2020, 2021). The SUNRISE (Submesoscales Under Near-Resonant Inertial Shear Experiment) program with observational and modeling components investigated submesoscale dynamics in this region. Strong frontal currents like the ACC can also modify submesoscale BI and eddy dynamics (Taylor et al. 2018, Stamper et al. 2018).

Small-scale turbulence can influence the fronts upon which submesoscales develop. In the absence of turbulence, we might anticipate that horizontal buoyancy gradients in the upper ocean will be balanced by a vertically sheared thermal wind. However, turbulence tends to homogenize momentum in addition to scalars. When turbulent mixing reduces the thermal wind shear, it leaves behind an unbalanced horizontal hydrostatic pressure gradient. This pressure gradient will drive

a vertically sheared cross-front flow that is part of the more general ageostrophic secondary circulation (Flament & Armi 2000, Cronin & Kessler 2009, Wenegrat & McPhaden 2016, McWilliams 2017).

In realistic simulations of the Gulf Stream region, Gula et al. (2014) found that the dominant terms in the horizontal momentum equations were the Coriolis acceleration, the hydrostatic pressure gradient, and the parameterized vertical mixing of momentum. They called the resulting state turbulent thermal wind (TTW) balance since the vertical mixing of momentum can be viewed as modifying thermal wind balance if the flow remains quasi-steady. They noted that the TTW circulation is frontogenetic and intensifies the horizontal density gradients within the dense filament near the ocean surface. Sullivan & McWilliams (2018) and Pham & Sarkar (2018) used large-eddy simulations to study the response of a density filament and front to small-scale turbulence. In both cases additional turbulence is generated as large density and velocity gradients develop at the sharpening filament or front, and this turbulence eventually arrests frontogenesis.

Although the TTW circulation intensifies density gradients at the ocean surface, when vertical mixing is maintained it can also cause the front to spread out horizontally through shear dispersion. When restratification by the vertically sheared cross-front TTW flow is counteracted by vertical mixing, the net result will be an effective horizontal spreading of the isopycnals (Young 1994; Crowe & Taylor 2018, 2019b). It remains unclear whether this process develops at submesoscale fronts where turbulence and submesoscales are highly coupled. Vertical mixing induced by small-scale turbulence reduces the growth rate of submesoscale BI (Young & Chen 1995, Crowe & Taylor 2019a), which might explain the lack of submesoscale features often observed in summer (Callies et al. 2015, Thompson et al. 2016). Together, these studies clearly demonstrate the complicated interactions between small-scale turbulence and submesoscale currents.

4.2. Large-Scale Impacts

Vertical fluxes of buoyancy and other tracers, arising from submesoscale motions, may also influence larger-scale components of the ocean circulation and Earth's climate. Modifications to the ocean's interior stratification linked to submesoscales may take many years to accrue, making simulations or observations of these larger-scale interactions challenging to obtain. However, evidence is growing that misrepresentation of submesoscale dynamics contributes to uncertainty in future climate predictions.

The submesoscale route to dissipation was discussed in Section 4.1, but other studies have highlighted that submesoscale BI, similar to its mesoscale counterpart, may also transfer energy to larger scales. As noted above, submesoscale KE is typically amplified in winter when MLs are deep and potential energy reservoirs are largest (Callies et al. 2015, Buckingham et al. 2016). Mesoscale KE, on the other hand, often peaks in spring, especially in western boundary currents. This cannot be explained by temporal fluctuations in the ocean's thermocline stratification, which varies on longer timescales. This led Sasaki et al. (2014) to propose that the spring mesoscale KE peak is created through up-scale energy transfer from the submesoscale.

Energy residing at submesoscales may undergo transfer to either larger or smaller scales, depending on local surface forcing and active submesoscale instabilities. Moored measurements in the North Atlantic (Naveira Garabato et al. 2022), using an assumption that energy transfers estimated in frequency space can be directly mapped to horizontal wavenumber space, indicated a change in the direction of energy transfer during the winter/spring transition. During winter, an active submesoscale eddy field generated by submesoscale BI supports an up-scale transfer of KE from submesoscale to mesoscale motions. Then, as the MLD decreases in early spring, the observations suggest a down-scale transfer of energy, attributed to enhanced frontogenesis by mesoscale

stirring. The observed down-scale energy transfer was not reproduced in a numerical model of the region with 2-km resolution, potentially due to the model's inability to represent sub-10-km frontogenesis. While the inherent limitations of this data set cause the statistical significance of the diagnosed energy transfers to be marginal at best, this study highlights the complex and likely spatially and temporally heterogeneous nature of energy transfer at submesoscales.

Numerous studies indicate that coarse-resolution general circulation models fail to reproduce MLDs, especially at subseasonal timescales (Belcher et al. 2012, Sallée et al. 2013, Damerell et al. 2020). Simulated MLs are biased too deep over most of the ocean in the winter, whereas simulated MLs are typically too shallow in the summer, especially in the Southern Ocean and the tropics (Fox-Kemper et al. 2021). The representation of submesoscale BI through an advective streamfunction (Equation 11) led to a dramatic and near-global reduction in MLD when implemented in both ocean-only and coupled climate models with a nominal 1° resolution (Fox-Kemper et al. 2011). The largest change in MLDs occurred in polar regions where MLs are deepest and the parameterization was most active. Overall, this representation of submesoscale motions significantly reduced deep-biased regions in these models with implications for ocean heat and carbon uptake.

The submesoscale parameterization also modified the global overturning circulation in these experiments. Most directly, the eddy streamfunction (Equation 11) made a substantial contribution to the global overturning with an ~ 10 -Sv volume transport, comparable to the interior Atlantic Meridional Overturning Circulation (Fox-Kemper et al. 2011). In models that explicitly resolve submesoscale eddies, the overturning is localized to sparse but strong fronts and does not have such a large magnitude. Still, submesoscales may influence the global overturning circulation through changes in the ocean's interior vertical stratification and isopycnal outcropping locations. ML restratification can influence the outcrop location and outcrop area of various density classes, altering the buoyancy flux experienced by these waters and thus water mass transformation rates that control the overturning strength (Groeskamp et al. 2019). Similarly, there is evidence that submesoscale eddies can induce restratification well below the ocean surface, especially in weakly stratified polar regions (e.g., Siegelman et al. 2020) and may even influence the formation of deep and bottom waters (Tagklis et al. 2020). Interactions among submesoscales, surface density distributions, and surface buoyancy fluxes require further exploration in submesoscale-resolving, coupled ocean-atmosphere models, which are at the frontier of climate modeling.

Vertical fluxes of heat and other tracers are amplified at submesoscales and typically dominate over fluxes at mesoscales and larger scales. Parameterization of submesoscale eddies was found to increase global mean SST by 0.1°C in most of the GCMs analyzed by Fox-Kemper et al. (2011). A more direct estimate of vertical heat fluxes related to submesoscale motions, occurring at 10- to 50-km scales, was produced using a global, $1/48^\circ$ -resolution (~ 2 km) ocean model (Su et al. 2018). The model output confirmed that submesoscale fluxes are up to five times larger than mesoscale fluxes, and that heat fluxes diagnosed at 40 m below the sea surface are systematically upward (positive). This positive heat flux is a signature of submesoscale BI (Section 3; **Figure 2**). Mean submesoscale heat fluxes in the wintertime mid-latitudes reached ~ 100 W/m^2 , with the largest magnitudes localized to regions of strong eddy stirring in western boundary currents and the Southern Ocean's ACC. While it is challenging to directly compare this simulation with lower-resolution models because of differences in air-sea fluxes, surface temperatures in the $1/48^\circ$ model were roughly 0.3°C warmer than in a $1/24^\circ$ model. Heat flux contributions from processes occurring at scales of 0.1–10 km were unresolved, but higher-resolution studies (e.g., Barkan et al. 2017) suggest that heat fluxes at these scales remain positive.

A limitation of the Su et al. (2018) study is the lack of coupling between the atmosphere and ocean. Surface winds, air temperature, and humidity, which help set air-sea fluxes, are prescribed in uncoupled models and do not respond to the formation of submesoscale fronts and eddies,

even if resolved by the ocean component. The impact of submesoscales on air–sea exchange is a compelling open question. Mesoscale eddies provide a wind–current feedback loop on the surface stress that modulates the air–sea transfer of momentum and leads to a reduction in mesoscale KE (Renault et al. 2017). Satellite measurements show a strong correlation between the wind stress curl and the ocean’s surface vorticity (Chelton & Xie 2010). Since vorticity is enhanced at submesoscales (e.g., $Ro \equiv \zeta/f \sim 1$), wind–current feedback loops and Ekman vertical velocities may strengthen at these smaller scales (Renault et al. 2018). Finally, early results from high-resolution coupled climate models suggest that submesoscale fronts can modulate atmospheric dynamics by modifying boundary layer turbulence over small scales (Wenegrat & Arthur 2018, Strobach et al. 2022).

Surface boundary layer processes play a critical role in ventilating the interior ocean and setting the properties of subducted water masses. Wenegrat et al. (2018) suggested that submesoscale motions impact the rate of formation of subtropical mode waters. Submesoscale BI, by restratifying the surface ocean, opposes the destruction of stratification and PV by strong surface cooling in this region; resolution of submesoscale motions was found to reduce PV removal by a factor of two. The impact of submesoscale motions on ocean ventilation is likely to be especially acute in the Southern Ocean where deep-ocean density classes outcrop at the surface. Balwada et al. (2018) carried out a suite of idealized circumpolar channel simulations and showed that steadily increasing the resolution from 20 km to 1 km produced two key results. First, MLs shoaled in the high-resolution simulations, which is consistent with more active submesoscale BI. Yet, despite the increased near-surface stratification, tracer concentrations were enhanced in the interior in the high-resolution runs. The 1-km simulation was found to take up 50% more tracer than the 20-km simulation. These results are consistent with observations that show enhanced surface–interior exchange due to submesoscale dynamics (Adams et al. 2017, Uchida et al. 2019), especially in regions where the ACC interacts with topography (Bachman & Klocker 2020, Dove et al. 2021).

A substantial literature exists on the influence of submesoscale tracer fluxes on biogeochemical cycling (e.g., Klein & Lapeyre 2009, Lévy et al. 2012, Mahadevan 2016). Early studies pointed to submesoscale upwelling events, setting the characteristic patchy distribution of primary productivity (Martin et al. 2002). However, later reviews have emphasized the challenge of determining whether this patchiness arises from small-scale, localized nutrient delivery or from passive mesoscale stirring of plankton populations that fluxes tracer variance to smaller scales (Lévy et al. 2018). The increased use of autonomous in situ instruments and towed oceanographic platforms has shown that submesoscales can contribute to the export of surface properties, such as particulate organic carbon, a process termed the eddy subduction pump (Boyd et al. 2019). The North Atlantic Bloom experiment has been particularly influential by suggesting that submesoscale motions contribute to the timing and magnitude of carbon export following the North Atlantic spring bloom (Mahadevan et al. 2012) and account for up to 50% of springtime carbon export in parts of the North Atlantic and Southern oceans (Omand et al. 2015). In recent years, a clearer picture has emerged that intermittent, strong subduction events develop at buoyancy fronts that form on the periphery of mesoscale and submesoscale eddies (Brannigan 2016, Taylor 2018, Ruiz et al. 2019, Freilich & Mahadevan 2021).

The influence of submesoscales on the large-scale ocean circulation and the climate system engenders a need to consider how submesoscales will change under global warming. This warming has been most pronounced at high latitudes, where surface ocean properties are closely tied to sea ice properties (e.g., concentration, extent, and thickness). Within the marginal ice zone, sea ice breaks into individual floes. As these floes melt, horizontal density gradients develop at the floe edge and generate mesoscale and submesoscale eddies through BI. These eddies

transport heat laterally under the ice floes and have a strong influence on melt rates (Horvat et al. 2016). Furthermore, mobile ice floes have a tendency to be trapped within submesoscale eddies and filaments when winds are weak (Manucharyan & Thompson 2017), which concentrates the variability of the ocean's surface heat flux at submesoscales (Manucharyan & Thompson 2022). Enhanced heating at submesoscales, which creates a more mobile sea-ice field, may constitute a missing positive feedback loop in climate models.

The role of submesoscales in a changing climate was directly addressed by Richards et al. (2021) in a series of submesoscale-resolving simulations for a region of the northeast Atlantic. Warming conditions led to shallower MLs and a decrease in mesoscale KE, which together reduced the near-surface vertical heat (buoyancy) flux. In simulations designed to suppress submesoscales, MLs shoaled to an even greater extent than in the submesoscale-permitting runs, emphasizing the importance of wind/front interactions in sustaining deep MLs (Section 4.1). The submesoscale-resolving runs experienced a reduction in mesoscale KE between present and warmer states that was twice as strong as in the simulations where submesoscales were suppressed, which the authors attributed to changes in nonlinear energy exchanges across these scales (**Figure 7**). Although many questions remain, the growing evidence for the influence of submesoscales on oceanic energetics and tracer fluxes suggests that accounting for submesoscales can improve the fidelity of global ocean and climate models. In particular, the influence of submesoscales on air-sea exchange remains relatively unexplored, despite the fact that these processes are likely to have a significant impact on ocean heat and carbon uptake.

SUMMARY POINTS

1. Submesoscale motions, of the order 200 m–20 km, are ubiquitous in the upper ocean and serve as a key intermediary between larger-scale balanced dynamics and unbalanced turbulence.
2. Submesoscales are energized by a variety of instabilities that develop from balanced currents.
3. Submesoscales leave an imprint on turbulence in the upper ocean through generation via shear instabilities at submesoscale fronts and via spatially heterogeneous restratification.
4. Energy residing at submesoscales may undergo transfer to either smaller dissipative scales via secondary instabilities and 3D turbulence, or larger scales via submesoscale restratification and nonlinear eddy dynamics.

FUTURE ISSUES

1. How do the direction and magnitude of the energy transfer through the submesoscale range vary in space and time and how does energy transfer contribute to the ocean's energy budget?
2. How do submesoscale instabilities influence the exchange of waters between the ocean surface and the interior? In particular, how does this process vary geographically and seasonally and how can it best be parameterized in ocean and climate models?
3. How can the influence of submesoscales on boundary layer turbulence be parameterized in large-scale ocean models?

4. How do submesoscales respond to coupled air–sea interactions and how does this coupling influence ocean heat and carbon uptake?
5. How do submesoscales influence the long-time equilibrium state of the ocean, as well as the ocean’s response to climate forcing?

DISCLOSURE STATEMENT

The authors are not aware of any biases that might be perceived as affecting the objectivity of this review.

ACKNOWLEDGMENTS

The authors are grateful to Baylor Fox-Kemper and an anonymous reviewer for helpful comments and suggestions.

LITERATURE CITED

- Adams KA, Hosegood P, Taylor JR, Sallée JB, Bachman S, et al. 2017. Frontal circulation and submesoscale variability during the formation of a Southern Ocean mesoscale eddy. *J. Phys. Ocean.* 47(7):1737–53
- Akitomo K. 2010. Baroclinic instability and submesoscale eddy formation in weakly stratified oceans under cooling. *J. Geophys. Res. Oceans* 115:C11027
- Bachman SD, Fox-Kemper B, Pearson B. 2017a. A scale-aware subgrid model for quasi-geostrophic turbulence. *J. Geophys. Res. Oceans* 122(2):1529–54
- Bachman SD, Fox-Kemper B, Taylor JR, Thomas LN. 2017b. Parameterization of frontal symmetric instabilities. I: theory for resolved fronts. *Ocean Model.* 109:72–95
- Bachman SD, Klocker A. 2020. Interaction of jets and submesoscale dynamics leads to rapid ocean ventilation. *J. Phys. Ocean.* 50(10):2873–83
- Badin G, Tandon A, Mahadevan A. 2011. Lateral mixing in the pycnocline by baroclinic mixed layer eddies. *J. Phys. Ocean.* 41(11):2080–101
- Balwada D, Smith KS, Abernathey R. 2018. Submesoscale vertical velocities enhance tracer subduction in an idealized Antarctic Circumpolar Current. *Geophys. Res. Lett.* 45(18):9790–802
- Barkan R, McWilliams JC, Shchepetkin AF, Molemaker MJ, Renault L, et al. 2017. Submesoscale dynamics in the northern Gulf of Mexico. Part I: regional and seasonal characterization and the role of river outflow. *J. Phys. Ocean.* 47(9):2325–46
- Barkan R, Molemaker MJ, Srinivasan K, McWilliams JC, D’Asaro EA. 2019. The role of horizontal divergence in submesoscale frontogenesis. *J. Phys. Ocean.* 49(6):1593–618
- Belcher SE, Grant AL, Hanley KE, Fox-Kemper B, Van Roekel L, et al. 2012. A global perspective on Langmuir turbulence in the ocean surface boundary layer. *Geophys. Res. Lett.* 39(18):L18605
- Blumen W. 1979. On short-wave baroclinic instability. *J. Atmos. Sci.* 36(10):1925–33
- Boccaletti G, Ferrari R, Fox-Kemper B. 2007. Mixed layer instabilities and restratification. *J. Phys. Ocean.* 37(9):2228–50
- Boyd PW, Claustre H, Lévy M, Siegel DA, Weber T. 2019. Multi-faceted particle pumps drive carbon sequestration in the ocean. *Nature* 568:327–35
- Brannigan L. 2016. Intense submesoscale upwelling in anticyclonic eddies. *Geophys. Res. Lett.* 43:3360–69
- Brannigan L, Marshall DP, Naveira-Garabato A, Nurser AG. 2015. The seasonal cycle of submesoscale flows. *Ocean Model.* 92:69–84
- Brüggemann N, Eden C. 2014. Evaluating different parameterizations for mixed layer eddy fluxes induced by baroclinic instability. *J. Phys. Oceanogr.* 44(9):2524–46

- Buckingham CE, Khaleel Z, Lazar A, Martin AP, Allen JT, et al. 2017. Testing Munk's hypothesis for submesoscale eddy generation using observations in the North Atlantic. *J. Geophys. Res. Oceans* 122(8):6725–45
- Buckingham CE, Lucas NS, Belcher SE, Rippeth TP, Grant ALM, et al. 2019. The contribution of surface and submesoscale processes to turbulence in the open ocean surface boundary layer. *J. Adv. Model. Earth Syst.* 11:4066–94
- Buckingham CE, Naveira Garabato AC, Thompson AF, Brannigan L, Lazar A, et al. 2016. Seasonality of submesoscale flows in the ocean surface boundary layer. *Geophys. Res. Lett.* 43(5):2118–26
- Callies J, Ferrari R. 2018a. Baroclinic instability in the presence of convection. *J. Phys. Ocean.* 48(1):45–60
- Callies J, Ferrari R. 2018b. Note on the rate of restratification in the baroclinic spin-down of fronts. *J. Phys. Ocean.* 48(7):1543–53
- Callies J, Ferrari R, Klymak JM, Gula J. 2015. Seasonality in submesoscale turbulence. *Nat. Commun.* 6:6862
- Callies J, Flierl G, Ferrari R, Fox-Kemper B. 2016. The role of mixed-layer instabilities in submesoscale turbulence. *J. Fluid Mech.* 788:5–41
- Canuto V, Dubovikov M. 2010. Mixed layer sub-mesoscale parameterization—part 1: derivation and assessment. *Ocean Sci.* 6(3):679–93
- Capet X, Campos E, Paiva A. 2008a. Submesoscale activity over the Argentinian shelf. *Geophys. Res. Lett.* 35(15):L15605
- Capet X, McWilliams JC, Molemaker MJ, Shchepetkin AF. 2008b. Mesoscale to submesoscale transition in the California Current System. Part I: flow structure, eddy flux, and observational tests. *J. Phys. Ocean.* 38:29–43
- Capet X, McWilliams JC, Molemaker MJ, Shchepetkin AF. 2008c. Mesoscale to submesoscale transition in the California Current System. Part III: energy balance and flux. *J. Phys. Ocean.* 38(10):2256–69
- Caulfield CP. 2021. Layering, instabilities, and mixing in turbulent stratified flows. *Annu. Rev. Fluid Mech.* 53:113–45
- Charney JG. 1947. The dynamics of long waves in a baroclinic westerly current. *J. Atmos. Sci.* 4(5):136–62
- Chelton DB, Xie SP. 2010. Coupled ocean-atmosphere interactions at oceanic mesoscales. *Oceanography* 23:52–69
- Cronin MF, Kessler WS. 2009. Near-surface shear flow in the tropical Pacific cold tongue front. *J. Phys. Oceanogr.* 39(5):1200–15
- Crowe MN, Taylor JR. 2018. The evolution of a front in turbulent thermal wind balance. Part 1. Theory. *J. Fluid Mech.* 850:179–211
- Crowe MN, Taylor JR. 2019a. Baroclinic instability with a simple model for vertical mixing. *J. Phys. Ocean.* 49(12):3273–300
- Crowe MN, Taylor JR. 2019b. The evolution of a front in turbulent thermal wind balance. Part 2. Numerical simulations. *J. Fluid Mech.* 880:326–52
- Damerell GM, Heywood KJ, Calvert D, Grant ALM, Bell MJ, Belcher SE. 2020. A comparison of five surface mixed layer models with a year of observations in the North Atlantic. *Prog. Oceanogr.* 187:102316
- D'Asaro E, Lee C, Rainville L, Harcourt R, Thomas L. 2011. Enhanced turbulence and energy dissipation at ocean fronts. *Science* 332(6027):318–22
- Dong J, Fox-Kemper B, Zhang H, Dong C. 2020. The scale of submesoscale baroclinic instability globally. *J. Phys. Oceanogr.* 50(9):2649–67
- Dong J, Fox-Kemper B, Zhang H, Dong C. 2021. The scale and activity of symmetric instability estimated from a global submesoscale-permitting ocean model. *J. Phys. Oceanogr.* 51(5):1655–70
- Dove LA, Thompson AF, Balwada D, Gray AR. 2021. Observational evidence for ventilation hotspots in the Southern Ocean. *J. Geophys. Res. Oceans* 126:e2021JC017178
- Eady ET. 1949. Long waves and cyclone waves. *Tellus* 1(3):33–52
- Eldevik T, Dysthe KB. 2002. Spiral eddies. *J. Phys. Ocean.* 32(3):851–69
- Evans DG, Lucas NS, Hemsley V, Frajka-Williams E, Naveira Garabato AC, et al. 2018. Annual cycle of turbulent dissipation estimated from seagliders. *Geophys. Res. Lett.* 45(19):10560–69
- Ferrari R, Wunsch C. 2009. Ocean circulation kinetic energy: reservoirs, sources, and sinks. *Annu. Rev. Fluid Mech.* 41:253–82

- Flament P, Armi L. 2000. The shear, convergence, and thermohaline structure of a front. *J. Phys. Ocean.* 30(1):51–66
- Follows MJ, Williams RG, Marshall JC. 1996. The solubility pump of carbon in the subtropical gyre of the North Atlantic. *J. Mar. Res.* 54(4):605–30
- Fox-Kemper B, Danabasoglu G, Ferrari R, Griffies S, Hallberg R, et al. 2011. Parameterization of mixed layer eddies. III: implementation and impact in global ocean climate simulations. *Ocean Model.* 39(1–2):61–78
- Fox-Kemper B, Ferrari R, Hallberg R. 2008. Parameterization of mixed layer eddies. Part I: theory and diagnosis. *J. Phys. Ocean.* 38(6):1145–65
- Fox-Kemper B, Hewitt HT, Xiao C, Aoalgeirsdóttir G, Drijfhout SS, et al. 2021. *Climate Change 2021: The Physical Science Basis. Contribution of Working Group I to the Sixth Assessment Report of the Intergovernmental Panel on Climate Change*. Cambridge, UK: Cambridge Univ. Press
- Freilich M, Mahadevan A. 2021. Coherent pathways for subduction from the surface mixed layer at ocean fronts. *J. Geophys. Res.* 126:e2020JC017042
- Griffiths RW, Killworth PD, Stern ME. 1982. Ageostrophic instability of ocean currents. *J. Fluid Mech.* 117:343–77
- Groeskamp S, Griffies SM, Iudicone D, Marsh R, Nurser AG, Zika JD. 2019. The water mass transformation framework for ocean physics and biogeochemistry. *Annu. Rev. Mar. Sci.* 11:271–305
- Gula J, Molemaker MJ, McWilliams JC. 2014. Submesoscale cold filaments in the Gulf Stream. *J. Phys. Ocean.* 44(10):2617–43
- Gula J, Molemaker MJ, McWilliams JC. 2016. Topographic generation of submesoscale centrifugal instability and energy dissipation. *Nat. Commun.* 7:12811
- Haine TW, Marshall J. 1998. Gravitational, symmetric, and baroclinic instability of the ocean mixed layer. *J. Phys. Ocean.* 28(4):634–58
- Hamlington PE, Van Roekel LP, Fox-Kemper B, Julien K, Chini GP. 2014. Langmuir–submesoscale interactions: descriptive analysis of multiscale frontal spindown simulations. *J. Phys. Ocean.* 44(9):2249–72
- Held IM, Pierrehumbert RT, Garner ST, Swanson KL. 1995. Surface quasi-geostrophic dynamics. *J. Fluid Mech.* 282:1–20
- Horvat C, Tziperman E, Campin JM. 2016. Interaction of sea ice floe size, ocean eddies, and sea ice melting. *Geophys. Res. Lett.* 43:8083–90
- Hoskins B. 1974. The role of potential vorticity in symmetric stability and instability. *Q. J. R. Meteorol. Soc.* 100(425):480–82
- Johnston TS, Rudnick DL, Pallàs-Sanz E. 2011. Elevated mixing at a front. *J. Geophys. Res. Oceans* 116:C11033
- Klein P, Hua BL, Lapeyre G, Capet X, Le Gentil S, Sasaki H. 2008. Upper ocean turbulence from high-resolution 3D simulations. *J. Phys. Ocean.* 38(8):1748–63
- Klein P, Lapeyre G. 2009. The oceanic vertical pump induced by mesoscale and submesoscale turbulence. *Annu. Rev. Mar. Sci.* 1:351–75
- Kundu PK, Cohen IM, Dowling DR. 2015. *Fluid Mechanics*. London: Academic
- Lapeyre G, Klein P. 2006. Dynamics of the upper oceanic layers in terms of surface quasigeostrophy theory. *J. Phys. Ocean.* 36(2):165–76
- Lapeyre G, Klein P, Hua BL. 2006. Oceanic restratification forced by surface frontogenesis. *J. Phys. Ocean.* 36(8):1577–90
- Lévy M, Ferrari R, Franks PJ, Martin AP, Rivière P. 2012. Bringing physics to life at the submesoscale. *Geophys. Res. Lett.* 39:L14602
- Lévy M, Franks PJS, Smith KS. 2018. The role of submesoscale currents in structuring marine ecosystems. *Nat. Commun.* 9:4758
- Lindborg E. 2006. The energy cascade in a strongly stratified fluid. *J. Fluid Mech.* 550:207–42
- Lorenz EN. 1955. Available potential energy and the maintenance of the general circulation. *Tellus* 7(2):157–167
- Mahadevan A. 2016. The impact of submesoscale physics on primary productivity of plankton. *Annu. Rev. Mar. Sci.* 8:161–84
- Mahadevan A, D’Asaro E, Lee C, Perry MJ. 2012. Eddy-driven stratification initiates North Atlantic spring phytoplankton blooms. *Science* 337(6090):54–58

- Mahadevan A, Olinger J, Street R. 1996. A nonhydrostatic mesoscale ocean model. Part I: well-posedness and scaling. *J. Phys. Ocean.* 26(9):1868–80
- Mahadevan A, Tandon A. 2006. An analysis of mechanisms for submesoscale vertical motion at ocean fronts. *Ocean Model.* 14(3–4):241–56
- Mahadevan A, Tandon A, Ferrari R. 2010. Rapid changes in mixed layer stratification driven by submesoscale instabilities and winds. *J. Geophys. Res. Oceans* 115:C03017
- Manucharyan GE, Thompson AF. 2017. Submesoscale sea ice-ocean interactions in marginal ice zones. *J. Geophys. Res.* 122:9455–75
- Manucharyan GE, Thompson AF. 2022. Heavy footprints of upper-ocean eddies on weakened Arctic sea ice in marginal ice zones. *Nat. Commun.* 13:2147
- Martin AP, Richards KJ, Bracco A, Provenzale A. 2002. Patchy productivity in the open ocean. *Glob. Biogeochem. Cycles* 16(2):9-1–9-9
- McWilliams JC. 1985. Submesoscale, coherent vortices in the ocean. *Rev. Geophys.* 23(2):165–82
- McWilliams JC. 2016. Submesoscale currents in the ocean. *Proc. R. Soc. A* 472(2189):20160117
- McWilliams JC. 2017. Submesoscale surface fronts and filaments: secondary circulation, buoyancy flux, and frontogenesis. *J. Fluid Mech.* 823:391–432
- McWilliams JC. 2019. A survey of submesoscale currents. *Geosci. Lett.* 6:3
- McWilliams JC, Molemaker MJ, Yavneh I. 2004. Ageostrophic, anticyclonic instability of a geostrophic, barotropic boundary current. *Phys. Fluids* 16(10):3720–25
- Mensa JA, Garraffo Z, Griffa A, Özgökmen TM, Haza A, Veneziani M. 2013. Seasonality of the submesoscale dynamics in the Gulf Stream region. *Ocean Dyn.* 63(8):923–41
- Molemaker MJ, McWilliams JC, Capet X. 2010. Balanced and unbalanced routes to dissipation in an equilibrated Eady flow. *J. Fluid Mech.* 654:35–63
- Molemaker MJ, McWilliams JC, Yavneh I. 2001. Instability and equilibration of centrifugally stable stratified Taylor-Couette flow. *Phys. Rev. Lett.* 86(23):5270–73
- Molemaker MJ, McWilliams JC, Yavneh I. 2005. Baroclinic instability and loss of balance. *J. Phys. Ocean.* 35(9):1505–17
- Munk W, Armi L, Fischer K, Zachariasen F. 2000. Spirals on the sea. *Proc. R. Soc. Lond. A* 456(1997):1217–80
- Naveira Garabato AC, Yu X, Callies J, Barkan R, Polzin KL, et al. 2022. Kinetic energy transfers between mesoscale and submesoscale motions in the open ocean's upper layers. *J. Phys. Ocean.* 52(1):75–97
- Omand MM, D'Asaro EA, Lee CM, Perry MJ, Briggs N, et al. 2015. Eddy-driven subduction exports particulate organic carbon from the spring bloom. *Science* 348(6231):222–25
- Pham HT, Sarkar S. 2018. Ageostrophic secondary circulation at a submesoscale front and the formation of gravity currents. *J. Phys. Ocean.* 48(10):2507–29
- Renault L, McWilliams JC, Gula J. 2018. Dampening of submesoscale currents by air-sea stress coupling in the Californian upwelling system. *Sci. Rep.* 8:13388
- Renault L, McWilliams JC, Masson S. 2017. Satellite observations of imprint of oceanic current on wind stress by air-sea coupling. *Sci. Rep.* 7:17747
- Richards KJ, Whitt DB, Brett G, Bryan FO, Feloy K, Long MC. 2021. The impact of climate change on ocean submesoscale activity. *J. Geophys. Res.* 126:e2020JC016750
- Riley JJ, Lelong MP. 2000. Fluid motions in the presence of strong stable stratification. *Annu. Rev. Fluid Mech.* 32:613–57
- Riley JJ, Lindborg E. 2008. Stratified turbulence: a possible interpretation of some geophysical turbulence measurements. *J. Atmos. Sci.* 65(7):2416–24
- Rudnick DL, Luyten JR. 1996. Intensive surveys of the Azores Front: 1. Tracers and dynamics. *J. Geophys. Res. Oceans* 101(C1):923–39
- Ruiz S, Claret M, Pascual A, Olita A, Troupin C, et al. 2019. Effects of oceanic mesoscale and submesoscale frontal processes on vertical transport of phytoplankton. *J. Geophys. Res.* 124(8):5999–6014
- Sallée JB, Shuckburgh E, Bruneau N, Meijers AJ, Bracegirdle TJ, Wang Z. 2013. Assessment of Southern Ocean mixed-layer depths in CMIP5 models: historical bias and forcing response. *J. Geophys. Res. Oceans* 118(4):1845–62
- Salmon R. 1980. Baroclinic instability and geostrophic turbulence. *Geophys. Astrophys. Fluid Dyn.* 15(1):167–211

- Sasaki H, Klein P, Qiu B, Sasai Y. 2014. Impact of oceanic-scale interactions on the seasonal modulation of ocean dynamics by the atmosphere. *Nat. Commun.* 5:5636
- Satomura T. 1981. An investigation of shear instability in a shallow water. *J. Meteorol. Soc. Japan Ser. II* 59(1):148–67
- Scully-Power P. 1986. *Navy oceanographer shuttle observations: STS 41-G mission report*. Tech. Doc. 7611, Nav. Underw. Syst. Cent., Newport, RI
- Shakespeare CJ. 2016. Curved density fronts: cyclogeostrophic adjustment and frontogenesis. *J. Phys. Oceanogr.* 46(10):3193–207
- Siegelman L, Klein P, Rivière P, Thompson AF, Torres HS, et al. 2020. Enhanced upward heat transport at deep submesoscale ocean fronts. *Nat. Geosci.* 13:50–55
- Skyllingstad ED, Duncombe J, Samelson RM. 2017. Baroclinic frontal instabilities and turbulent mixing in the surface boundary layer. Part II: forced simulations. *J. Phys. Ocean.* 47(10):2429–54
- Skyllingstad ED, Samelson R. 2012. Baroclinic frontal instabilities and turbulent mixing in the surface boundary layer. Part I: unforced simulations. *J. Phys. Ocean.* 42(10):1701–16
- Stamper MA, Taylor JR. 2017. The transition from symmetric to baroclinic instability in the Eady model. *Ocean Dyn.* 67:65–80
- Stamper MA, Taylor JR, Fox-Kemper B. 2018. The growth and saturation of submesoscale instabilities in the presence of a barotropic jet. *J. Phys. Ocean.* 48(11):2779–97
- Stone PH. 1966. On non-geostrophic baroclinic stability. *J. Atmos. Sci.* 23(4):390–400
- Stone PH. 1970. On non-geostrophic baroclinic stability: part II. *J. Atmos. Sci.* 27(5):721–26
- Stone PH. 1972. On non-geostrophic baroclinic stability: part III. The momentum and heat transports. *J. Atmos. Sci.* 29(3):419–26
- Strobach E, Klein P, Molod A, Fahad AA, Trayanov A, et al. 2022. Local air-sea interactions at ocean mesoscale and submesoscale in a western boundary current. *Geophys. Res. Lett.* 49:e2021GL097003
- Su Z, Wang J, Klein P, Thompson AF, Menemenlis D. 2018. Ocean submesoscales as a key component of the global heat budget. *Nat. Commun.* 9:775
- Sullivan PP, McWilliams JC. 2018. Frontogenesis and frontal arrest of a dense filament in the oceanic surface boundary layer. *J. Fluid Mech.* 837:341–80
- Sutherland BR, Achatz U, Caulfield CP, Klymak JM. 2019. Recent progress in modeling imbalance in the atmosphere and ocean. *Phys. Rev. Fluids* 4:010501
- Tagklis F, Bracco A, Ito T, Castelao R. 2020. Submesoscale modulation of deep water formation in the Labrador Sea. *Sci. Rep.* 10:17489
- Taylor JR. 2016. Turbulent mixing, restratification, and phytoplankton growth at a submesoscale eddy. *Geophys. Res. Lett.* 43(11):5784–92
- Taylor JR. 2018. Accumulation and subduction of buoyant material at submesoscale fronts. *J. Phys. Ocean.* 48(6):1233–41
- Taylor JR, Bachman S, Stamper M, Hosegood P, Adams K, et al. 2018. Submesoscale Rossby waves on the Antarctic Circumpolar Current. *Sci. Adv.* 4(3):eaao2824
- Taylor JR, Ferrari R. 2009. On the equilibration of a symmetrically unstable front via a secondary shear instability. *J. Fluid Mech.* 622:103–13
- Taylor JR, Ferrari R. 2010. Buoyancy and wind-driven convection at mixed layer density fronts. *J. Phys. Ocean.* 40(6):1222–42
- Taylor JR, Ferrari R. 2011. Ocean fronts trigger high latitude phytoplankton blooms. *Geophys. Res. Lett.* 38(23):L23601
- Taylor JR, Smith KM, Vreugdenhil CA. 2020. The influence of submesoscales and vertical mixing on the export of sinking tracers in large-eddy simulations. *J. Phys. Ocean.* 50(5):1319–39
- Thomas LN. 2005. Destruction of potential vorticity by winds. *J. Phys. Ocean.* 35(12):2457–66
- Thomas LN, Tandon A, Mahadevan A. 2008. Submesoscale processes and dynamics. In *Ocean Modeling in an Eddying Regime*, ed. MW Hecht, H Hasumi, pp. 17–38. Geophys. Monogr. Ser. 177. Washington, DC: Am. Geophys. Union
- Thomas LN, Taylor JR, D’Asaro EA, Lee CM, Klymak JM, Shcherbina A. 2016. Symmetric instability, inertial oscillations, and turbulence at the Gulf Stream front. *J. Phys. Ocean.* 46(1):197–217

- Thomas LN, Taylor JR, Ferrari R, Joyce TM. 2013. Symmetric instability in the Gulf Stream. *Deep Sea Res. II* 91:96–110
- Thompson AF, Lazar A, Buckingham C, Garabato ACN, Damerell GM, Heywood KJ. 2016. Open-ocean submesoscale motions: a full seasonal cycle of mixed layer instabilities from gliders. *J. Phys. Ocean.* 46(4):1285–307
- Thorpe A, Rotunno R. 1989. Nonlinear aspects of symmetric instability. *J. Atmos. Sci.* 46(9):1285–99
- Tulloch R, Marshall J, Hill C, Smith KS. 2011. Scales, growth rates, and spectral fluxes of baroclinic instability in the ocean. *J. Phys. Ocean.* 41(6):1057–76
- Uchida T, Balwada D, Abernathy R, McKinley G, Smith S, Lévy M. 2019. The contribution of submesoscale over mesoscale eddy iron transport in the open Southern Ocean. *J. Adv. Model. Earth Syst.* 11:3934–58
- Verma V, Pham HT, Sarkar S. 2019. The submesoscale, the finescale and their interaction at a mixed layer front. *Ocean Model.* 140:101400
- Verma V, Pham HT, Sarkar S. 2022. Interaction between upper-ocean submesoscale currents and convective turbulence. *J. Phys. Oceanogr.* 52(3):437–58
- Wenegrat JO, Arthur R. 2018. Response of the atmospheric boundary layer to submesoscale sea surface temperature fronts. *Geophys. Res. Lett.* 45(24):13505–12
- Wenegrat JO, McPhaden MJ. 2016. Wind, waves, and fronts: frictional effects in a generalized Ekman model. *J. Phys. Ocean.* 46(2):371–94
- Wenegrat JO, Thomas LN, Gula J, McWilliams JC. 2018. Effects of the submesoscale on the potential vorticity budget of ocean mode waters. *J. Phys. Ocean.* 48(9):2141–65
- Whitt DB, Lévy M, Taylor JR. 2019. Submesoscales enhance storm-driven vertical mixing of nutrients: insights from a biogeochemical large eddy simulation. *J. Geophys. Res. Oceans* 124(11):8140–65
- Whitt DB, Taylor JR. 2017. Energetic submesoscales maintain strong mixed layer stratification during an autumn storm. *J. Phys. Ocean.* 47(10):2419–27
- Winters KB, Lombard PN, Riley JJ, D’Asaro EA. 1995. Available potential energy and mixing in density-stratified fluids. *J. Fluid Mech.* 289:115–28
- Wunsch C, Ferrari R. 2004. Vertical mixing, energy, and the general circulation of the oceans. *Annu. Rev. Fluid Mech.* 36:281–314
- Yavneh I, McWilliams JC, Molemaker MJ. 2001. Non-axisymmetric instability of centrifugally stable stratified Taylor-Couette flow. *J. Fluid Mech.* 448:1–21
- Young W. 1994. The subinertial mixed layer approximation. *J. Phys. Ocean.* 24(8):1812–26
- Young W, Chen L. 1995. Baroclinic instability and thermohaline gradient alignment in the mixed layer. *J. Phys. Ocean.* 25(12):3172–85